# Demodulation Contrast simulation for indirect Time-of-Flight sensors based on Fast Photo-Diode

G. Mugny*§, P. Fonteneau†§, B. Rodrigues-Goncalves†, J.M. Melo Santos‡, M. Vignetti†, C. Tubert*,
A. Crocherie†, D. Rideau†, F. Lalanne†, V. Farys† and A. Tournier†

* STMicroelectronics, 12 Rue Jules Horowitz, 38019 Grenoble, France
Tel: +44 131 558 4020; Email: gabriel.mugny@st.com
† STMicroelectronics, 850 rue J. Monnet, 38926 Crolles, France
‡ STMicroelectronics, 1, Tanfield, Inverleith Row, Edinburgh EH3 5DA, Scotland, UK
§ These authors contributed equally to this work.

*Abstract*—In this paper, the electrical and optical performances of an indirect Time-Of-Flight (iTOF) pixel based on fast photo-diode (FPD) are studied, by mean of TCAD and FDTD simulation. Key parameters are extracted, such as the demodulation contrast (DMC), quantum efficiency (QE) and parasitic light sensitivy (PLS) and their optimization discussed, in term of Si epitaxial layer (EPI) thickness, doping profile or optical diffractive structures.

## I. INTRODUCTION

iTOF sensors have been considered intensively in the literature for 3D depth map applications [1]. The number of recent publications and product releases show the great interest of industry for these devices in mobile applications, for high resolution, low power consumption purpose and intermediate level of image processing [2], [3], [4], [5]. To reach mm depth accuracy, the FPD must demodulate the photogenerated carriers at few hundreds of MHz. The high frequency 2-tap charge transfer efficiency (CTE) is commonly measured through the DMC. The latter must be predicted as efficiently as possible by simulation for pixel trials and performance improvement.

Lateral transfer has been intensively studied in the literature [6], and the role of depth transfer in small pixels has been recently highlighted [5]. Recent work on Global-Shutter PD also showed that an accurate description of the optical propagation is required in small pixel working in near-infrared (NIR) wavelength [7].

In this paper, the transient collection of photogenerated carriers from the photo-diode into the memory is studied by mean of transient drift-diffusion simulation (using a commercial TCAD solver [8]) coupled to optical generation rate computed from a commercial FDTD solver [9].

## II. METHODOLOGY

### A. Pixel description

The pixel simulated is a 4.6$\mu$m pitch, back-side-illuminated (BSI) iTOF FPD pixel with two memory nodes (Fig. 1). It is composed of two transfer gates (TGMEM), two read-out gates and one single anti-blooming gate [2]. The same pixel design is used for all simulation, with process variation in term of diffractive structure, EPI thickness and doping implants.
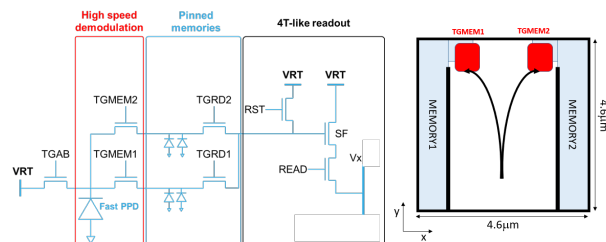


Fig. 1. (Left) Schematic of the iTOF FPD pixel. (Right) Basic pixel layout. The arrows show the transfer of electron from the FPD (white) towards TGMEM (red) and memories (cyan). Solid black lines represent deep trench isolation.

The carrier transfer speed is controlled by two different contributions: surfacic ("horizontal") and in depth ("vertical"). The horizontal electric field is created by shallow implants [10], [6], while vertical static electric field is created with gradual doping epitaxy and deep diode implants. The fine control of this static electric field is key to increase the transfer speed, while keeping power consumption low.

### B. Optical simulation

The light propagation in the optical stack of the pixel is computed with FDTD method, solving Maxwell equations on a finite-difference mesh.

The optical stack is optimized for application at 940nm, in term of microlens profile, underlayer thickness and anti-reflective coating. The external QE and PLS are extracted by integrating the optical absorption over the FPD and memory volumes. All results presented are averaged over a narrow bandwidth of 40nm to smooth interference effects coming from the Si cavity.

### C. Electrical simulation

The optical generation rate is then interpolated into the finite-element mesh used by the TCAD solver, through an *in-house* script [11].

Transient drift-diffusion equations coupled with Poisson equation are then solved on a process-calibrated 3D pixel structure. Ions implantation and diffusion models are calibrated on SIMS measurement.

## D. DMC extraction

The DMC can be computed from the convolution of the sinusoidal illumination wave with the response of the pixel to a LASER impulse - the Impulse Response Time (IRT). Experimentally, the pixel IRT is commonly measured with a short-pulse LASER illumination (typically $<100ps$), on which a delay is applied (see Fig. 2 and Ref. [12]).
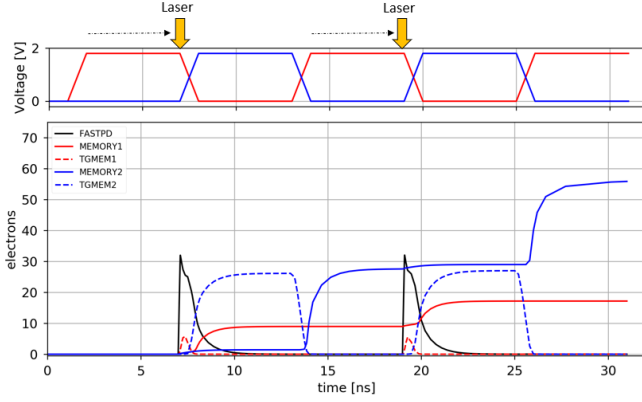


Fig. 2. Timing diagram for IRT extraction. Up: signal toggling the TGMEM1 (red) and TGMEM2 (blue) gates, showing the position of the LASER pulse (yellow arrow) and delay applied (black arrow). Down: integrated carrier concentration in different regions of the device as a function of time.
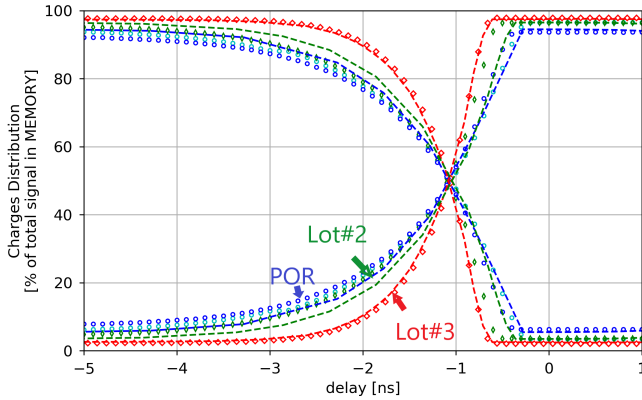


Fig. 3. Charge distribution in each memories at the end of the simulation/measurement, as a function of delay applied to the LASER, for the different implants cases shown in Fig. 9. Simulations are shown in lines, while measurement data are shown with symbols. Excellent match is observed. Note: the zero reference for the delay axis is arbitrary and the curves have been shifted to align the transition point between MEM1 and MEM2.

The charge distribution diagram as a function of the delay applied (see Fig. 3) allows to extract the IRT at low frequency (typically $\sim$10MHz), as well as extrapolate the high frequencies response, through the equation:

$$IRT_{exp}(f) = \frac{n_1(t_f) - n_2(t_f)}{n_1(t_f) + n_2(t_f)} \qquad (1)$$

where $n_1$ and $n_2$ are the number of electrons under MEM1 and MEM2 respectively and $t_f = t_0 + 1/(2f)$ is the toggling time corresponding to a given frequency $f$. The reference time

$t_0$ corresponds to the position where the two TGMEM toggle, and can be ill-defined for non-zero rise time and fall time. Moreover, this method requires many acquisitions, making it time- and resource-costly.

TCAD allows to extract the same information from a single simulation, by looking at the carrier concentration inside different zones of the pixel, as shown of Fig. 4. From the transient concentration of carriers under the TGMEM (green curve in Fig. 4), we can extract the IRT at different frequencies, writing Eq. 1 as:

$$IRT_{simu}(f) = \frac{2n_1(t_f) - n_{max}}{n_{max}} \qquad (2)$$

where $n_{max}$ is the maximum carrier concentration achieved under TGMEM at low frequency. We considered here $n_2 = n_{max} - n_1$ and the ideal case without PLS. $t_0$ is the non-ambiguous position of the very short LASER pulse.
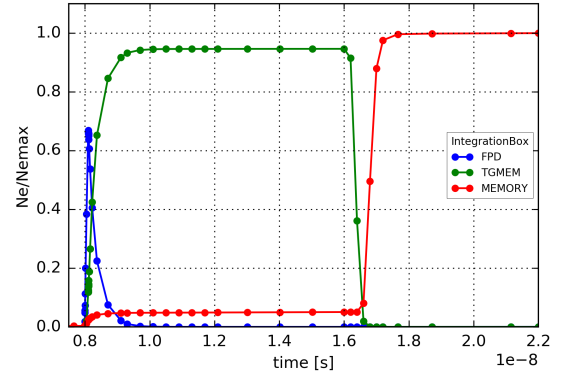


Fig. 4. Integrated carrier concentration in different regions of the device as a function of time (pulse of light is generated at $8ns$ and TGMEM is switched OFF at $16ns$).

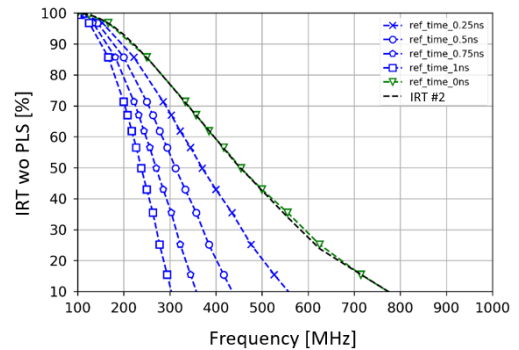The IRT extracted from these two methods is shown in Fig. 5, showing that they are equivalent.



Fig. 5. IRT extracted from TCAD simulation from Eq. 1 (green line) and Eq. 2 (black line). Here, a sharp rise time of 100ps is used, and good agreement is found between both methods. Blue curves show the impact of small variation on the $t_0$ reference time in Eq. 1.

## III. RESULTS

### A. EPI thickness

QE, PLS and IRT are extracted for different EPI thicknesses. As shown in Figs 6 and 7, while QE increases nearly linearly with EPI thickness, the IRT decreases significantly when EPI is increased. This is mainly due to the smaller static electric field achievable for higher EPI, as well as the increase in transfer distance for carrier generated near the BSI interface.
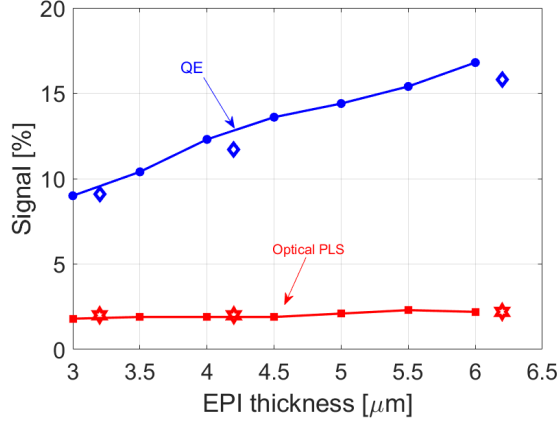


Fig. 6. Comparison of simulated (lines) and measured (symbols) QE (blue) and PLS (red) versus EPI thickness. No diffractive structure is included here.
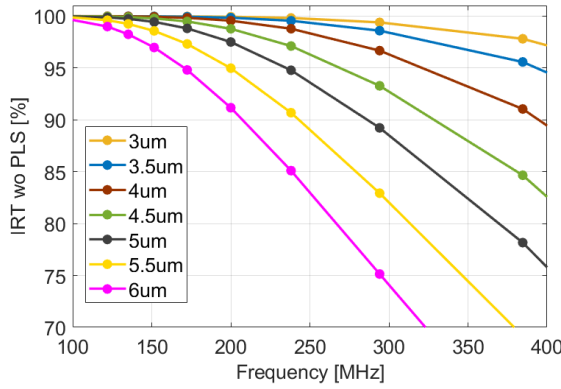


Fig. 7. Simulated IRT without PLS as a function of frequency of operation extracted with Eq. (2) for different EPI thicknesses.

There is thus a trade-off to find between QE and IRT. For device performance, the following Figure of Merit [13] can be considered: $FoM = \sqrt{QE} \cdot DMC \cdot f$. Fig. 8 shows that the optimal EPI depends on the choice for the frequency of operation: for that particular pixel, $6\mu$m EPI is optimum up to 200MHz, while thinner EPI should be favored for higher frequencies. Note that optical PLS is not affected by the change in EPI thickness and remains around 2%.

### B. Gradual epitaxy and deep diode doping: boosting the IRT

In order to further improve the depth transfer for thick EPI, a deep implant is introduced (Fig. 9), and both the gradual EPI profile and deep implant dose are optimized by simulation.
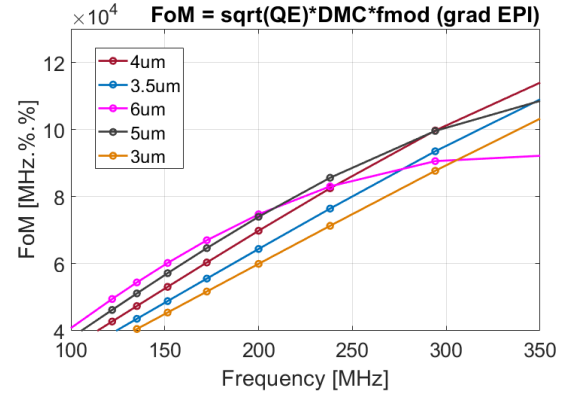


Fig. 8. Simulated figure of merit (see text and title) as a function of frequency for different EPI thicknesses. Simulated QE values of Fig. 6 are used.

Results in Fig. 10 show that both parameters are interdependent and thus need to be optimized at the same time. It also shows the important role of depth transfer on the IRT performances and that IRT higher than 90% at 300MHz is achieved after such optimization.
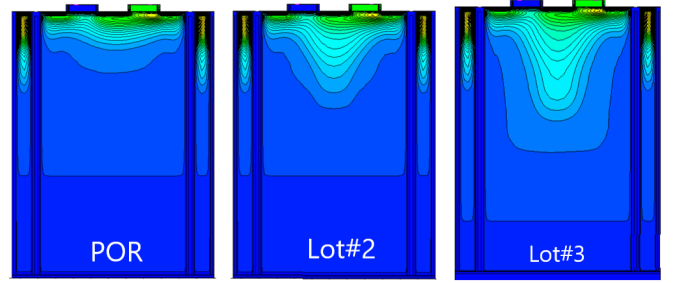


Fig. 9. (y,z) cross section of the electric potential in the middle of the FPD, for three different cases: (left) linear gradual doping with standard implants, (middle) linear gradual doping with optimized deep implants and (right) optimization of both gradual doping and deep diode implant. EPI thickness is $6\mu$m in the three cases.
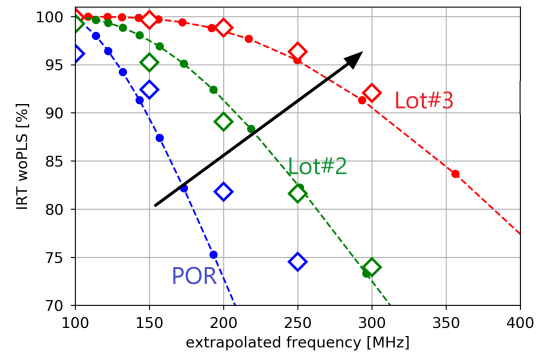


Fig. 10. Simulated (line) versus measured (symbols) IRT as a function of the frequency for the different implants cases shown in Fig. 9.

By introducing a second deep implant (not shown here), the gain is further increased up to 98% IRT, translating into a DMC of 77% at 300MHz (Table II).

The measured QE is slightly improved with the optimal doping profile, due to better extraction of charges, and reaches 18.5%.

### C. Diffractive structures: boosting the QE

Finally, diffractive structure is patterned on the back interface in order to increase QE. Both wet etched (inverted pyramids) and dry etched (trenches) structures are considered and their dimension, number and spacing optimized. Dry etched horizontal trenches allow to select a preferential direction of diffraction perpendicular to the memory region, allowing to keep PLS relatively low, while increasing QE up to 25% (Tables I and II). Our simulation also showed that, unlike EPI thickness, diffractive structures have no negative impact on DMC (not shown here).
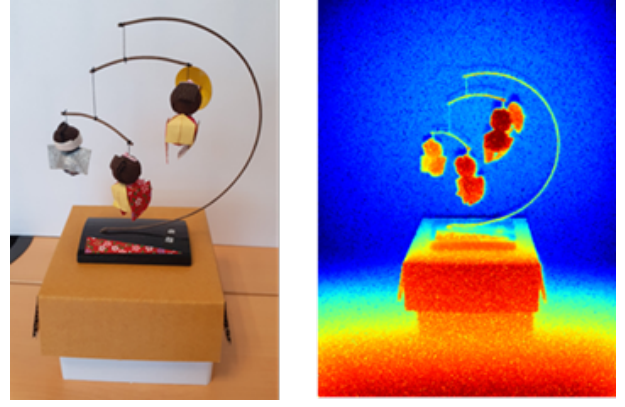


Fig. 11. 3D depth-map (right) of a mobile scene (left) obtained by a product built on the presented iTOF FPD pixel.



|  | No Struct. | Pyramid | Trench |
|---|---|---|---|
| QE (%) | 17.9 | 25.7 | 24.5 |
| PLS (%) | 2.8 | 14.0 | 6.5 |

TABLE I

TOP: TOP-VIEW OF THE DIFFRACTIVE STRUCTURES LAYOUT: WET ETCHED INVERSE PYRAMID (LEFT) AND DRY ETCHED HORIZONTAL TRENCH (RIGHT). BOTTOM: SIMULATED QE AND PLS VALUES AT 940NM.

Finally, this study allowed the development of a novel iTOF pixel and full system with performance at the State-of-the-Art (Table II and Fig. 11). Experimental data are shown in Figs. 6 and 10 and an excellent agreement with simulation is shown.

|  | This work | | Samsung [5] | Sony [4] | Microsoft [3] |
|---|---|---|---|---|---|
| Pitch ($\mu$m) | 4.6 | | 3.5 | 3.5 | 3.5 |
| QE (%) | 25 | | 38 | 32 | 25 |
| IRT (%) | 98 | 99 | - | - | - |
| DMC (%) | 77 | 88 | 80 | 79 | 87 |
| $f$ (MHz) | 300 | 200 | 200 | 200 | 200 |
| FoM (a.u.) | 1.2e5 | 8.8e4 | 9.9e4 | 8.9e4 | 8.7e4 |

TABLE II

PERFORMANCE COMPARISON BETWEEN OUR STUDY AND OTHER STUDIES IN THE LITERATURE.

## IV. CONCLUSION

This paper shows a complete and robust simulation methodology for the extraction of all important metrics for an iTOF pixel. The important role of depth transfer is highlighted, and the trade-off between QE and DMC is discussed.

This methodology can be applied to any other iTOF device, such as CAPD.

## ACKNOWLEDGMENT

## REFERENCES

[1] F. Remondino and D. Stoppa. Springer, 2013, vol. 68121.
[2] B. Rodrigues *et al.*, in *Proc. IISW*, 2017, pp. 266–269.
[3] C. S. Bamji *et al.*, in *2018 IEEE Proc. ISSCC*, 2018, pp. 94–96.
[4] Y. Ebiko *et al.*, in *2020 IEEE Proc. IEDM*. IEEE, 2020, pp. 33–1.
[5] M.-S. Keel *et al.*, in *2021 IEEE Proc. ISSCC*, vol. 64, 2021, pp. 106–108.
[6] F. Acerbi *et al.*, *IEEE Journal of the Electron Devices Society*, 2018.
[7] F. Pace *et al.*, in *2019 Proc. SISPAD*. IEEE, 2019, pp. 1–4.
[8] S. Device, *Inc., M-2016.12 edition*, 2016.
[9] . Lumerical, *Inc., 2019-r6 edition*, 2019.
[10] C. Tubert *et al.*, in *Proc. IISW*, 2009, pp. 1–3.
[11] A. Crocherie *et al.*, in *Proc. IISW*, 2009.
[12] B. Rodrigues Goncalves, Ph.D. dissertation, Lyon, 2016.
[13] Y. Kato *et al.*, *IEEE Journal of Solid-State Circuits*, pp. 1071–1078, 2018.